Structures of Competitive Inhibitor Complexes of Protocatechuate 3,4-Dioxygenase: Multiple Exogenous Ligand Binding Orientations within the Active Site[†,‡]

Allen M. Orville,[§] Natesan Elango, John D. Lipscomb, and Douglas H. Ohlendorf*

Department of Biochemistry, Medical School, and Center for Metals in Biocatalysis, University of Minnesota, Minneapolis, Minnesota 55455-0347

Received February 28, 1997; Revised Manuscript Received June 16, 1997[⊗]

ABSTRACT: Protocatechuate 3,4-dioxygenase (3,4-PCD) catalyzes the oxidative ring cleavage of 3,4-dihydroxybenzoate to produce β-carboxy-*cis*,*cis*-muconate. Crystal structures of *Pseudomonas putida* 3,4-PCD [quaternary structure of $(\alpha\beta Fe^{3+})_{12}$] complexed with seven competitive inhibitors [3-hydroxyphenylacetate (MHP), 4-hydroxyphenylacetate (PHP), 3-hydroxybenzoate (MHB), 4-hydroxybenzoate (PHB), 3-fluoro-4-hydroxybenzoate (FHB), 3-chloro-4-hydroxybenzoate (CHB), and 3-iodo-4-hydroxybenzoate (IHB)] are reported at 2.0−2.2 Å resolution with *R*-factors of 0.159−0.179. The inhibitors bind in a narrow active site crevasse lined with residues that provide a microenvironment that closely matches the chemical characteristics of the inhibitors. This results in as little as 20% solvent-exposed surface area for the higher-affinity inhibitors (PHB, CHB, and FHB). In uncomplexed 3,4-PCD, the active site Fe^{3+} is bound at the bottom of the active site crevasse by four endogenous ligands and a solvent molecule (Wat827). The orientations of the endogenous ligands are relatively unperturbed in each inhibitor complex, but the inhibitors themselves bind to or near the iron in a range of positions, all of which perturb the position of Wat827. The three lowest-affinity inhibitors (MHP, PHP, and IHB) yield distorted trigonal bipyramidal iron coordination geometry in which the inhibitor C4-phenolate group displaces the solvent ligand. MHB binds within the active site, but neither its C3-OH group nor the solvent molecule binds to the iron. The C4-phenolate group of the three highest-affinity inhibitors (PHB, CHB, and FHB) coordinates the Fe^{3+} adjacent to Wat827, resulting in a shift in its position to yield a six-coordinate distorted octahedral geometry. The range of inhibitor orientations may mimic the mechanistically significant stages of substrate binding to 3,4-PCD. The structure of the final substrate complex is reported in the following paper [Orville, A. M., Lipscomb, J. D., & Ohlendorf, D. H. (1997) *Biochemistry 36,* 10052−10066].

Protocatechuate 3,4-dioxygenase (3,4-PCD)[1] catalyzes the cleavage of O_2 and the concomitant ring opening of 3,4-dihydroxybenzoate (PCA) or related catecholic compounds to yield *cis*,*cis*-muconate products [for a review, see Lipscomb and Orville (1992)]. The enzyme has been isolated from many divergent soil bacteria and is regarded as the prototypical Fe^{3+} catecholic dioxygenase due to the fact that (i) more spectroscopic, kinetic, and mechanistic studies have been conducted for 3,4-PCD than for any other Fe^{3+} dioxygenase [for reviews, see Que (1989, 1993), Lipscomb and Orville (1992), and Que and Ho (1996)], (ii) overexpression and mutagenesis systems have been developed (Frazee et al., 1993; R. W. Frazee and J. D. Lipscomb, unpublished; C. A. Earhart and D. H. Ohlendorf, unpublished), and (iii) the high-resolution crystal structure has been solved (Ohlendorf et al., 1987, 1988, 1994). 3,4-PCD isolated from *Pseudomonas putida*[2] is a large aggregate (587 kDa) of 12 protomers, each composed of an α- and β-subunit and an Fe^{3+} ion bound in the β-subunit at the α-subunit−β-subunit interface. The tetrahedon-shaped molecule (Figure 1a) reflects the local *23(T)* symmetry with three orthogonal 2-fold and four 3-fold symmetry axes.

The catalytically essential ferric ion within each protomer delineates the active site in a cleft at the α-subunit−β-subunit interface which opens to the exterior of the holoenzyme. The walls of the active site cleft are formed primarily by residues from the α- and β-subunits within each protomer, although portions of the outer rim are composed of residues from 2-fold and 3-fold related protomers. Two tyrosinates (Tyr408 and Tyr447),[3] two histidines ($His460^{N\epsilon 2}$ and $His462^{N\epsilon 2}$), and an exogenous solvent molecule (Wat827), thought to be a

[†] This work was supported by grants from the National Institutes of Health to D.H.O. (GM-46436) and to J.D.L. (GM-24689). A.M.O. acknowledges a NIH predoctoral training grant (GM-07323) and a Doctoral Dissertation Fellowship from the Graduate School of the University of Minnesota.

[‡] The coordinates for the 3,4-PCD·inhibitor complexes have been deposited in the Brookhaven Protein Data Bank (Bernstein et al., 1977) with the following identifiers: 3,4-PCD·MHP, 3PCE; 3,4-PCD·PHP, 3PCG; 3,4-PCD·PHB, 3PCC; 3,4-PCD·MHB, 3PCB; 3,4-PCD·FHB, 3PCF; 3,4-PCD·CHB, 3PCH; and 3,4-PCD·IHB, 3PCI.

* Corresponding author: Douglas H. Ohlendorf, 4-225 Millard Hall, Department of Biochemistry, Medical School, University of Minnesota, Minneapolis, MN 55455-0347. Telephone: (612) 624-8436. Fax: (612) 625-2163. E-mail: ohlen@dccc.med.umn.edu.

[§] Current address: Institute of Molecular Biology, University of Oregon, Eugene, OR 97403.

[⊗] Abstract published in *Advance ACS Abstracts,* August 1, 1997.

[1] Abbreviations: 3,4-PCD, protocatechuate 3,4-dioxygenase; PCA, protocatechuate or 3,4-dihydroxybenzoate; MHB, *m*-hydroxybenzoate; PHB, *p*-hydroxybenzoate; MHP, *m*-hydroxyphenylacetate; PHP, *p*-hydroxyphenylacetate; FHB, 3-fluoro-4-hydroxybenzoate; CHB, 3-chloro-4-hydroxybenzoate; IHB, 3-iodo-4-hydroxybenzoate; EPR, electron paramagnetic resonance; LMCT, ligand to metal charge transfer; rms, root mean squared; F_P and $F_{P\cdot I}$, observed structure factors for the uncomplexed 3,4-PCD and the enzyme·inhibitor complexes, respectively.

[2] American Type Culture Collection (ATCC) 23975, previously classified as *Pseudomonas aeruginosa.*

S0006-2960(97)00468-6 CCC: $14.00

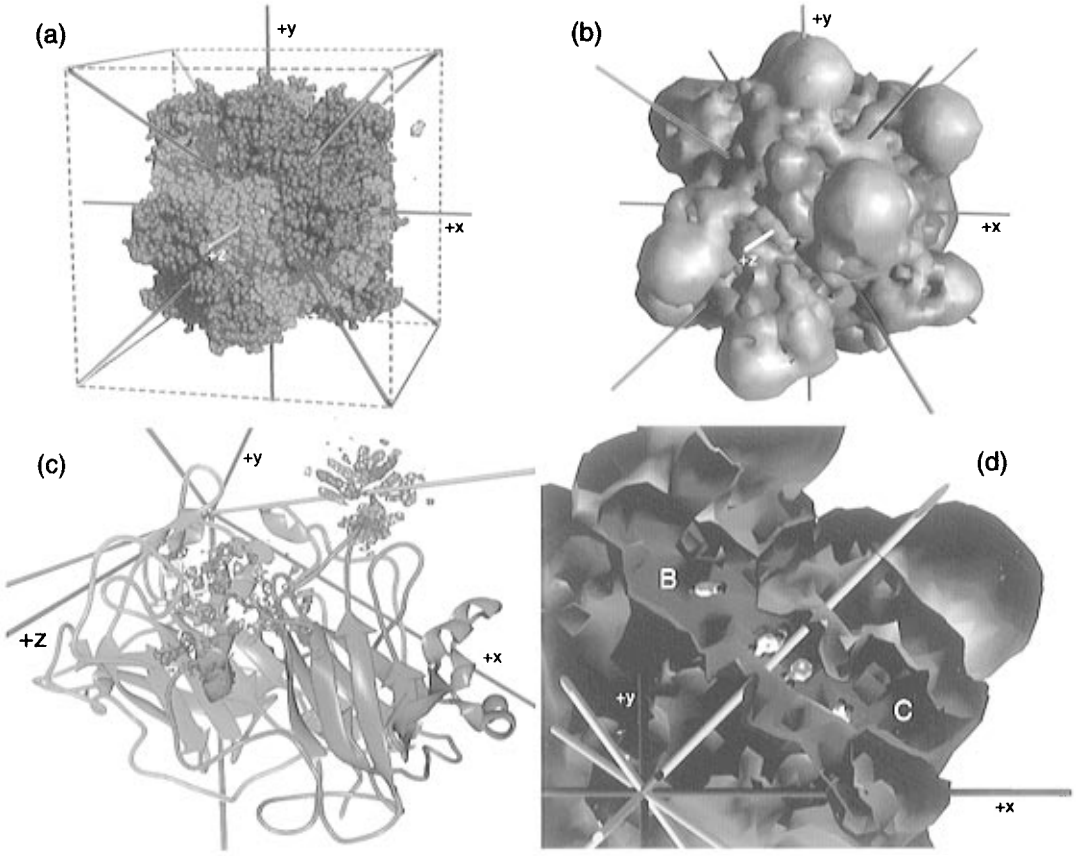

FIGURE 1: Topological overview of the *P. putida* 3,4-PCD structure. (a) Superposition of the *23(T)* symmetry elements on a space filling model of the $(\alpha\beta Fe^{3+})_{12}$ holoenzyme. The α- and *β*-subunits are shown in red and green, respectively. The outer limit of the active site in protomer A is near the $+z$ symmetry axis (white atoms). The 2-fold axes are labeled as $+x$, $+y$ (blue), and $+z$ (white). The 3-fold axes are shown in yellow with apical ends terminating at 1, 1, 1 (x, y, z) or -1, -1, 1 ($-x$, $-y$, z) and basal ends terminating at -1, 1, 1 ($-x$, y, z) or 1, -1, 1 (x, $-y$, z). Space filling models of PCA and Fe^{3+} are shown in the *x*/*y* plane to the right of the holoenzyme. (b) The calculated electrostatic isopotential (0.1 M salt solution) at $+1$ kT (blue) and -1 kT (red) superimposed on the holoenzyme in the same orientation and scale as in part a. (c) Initial difference density (5−2.2 Å resolution) for the 3,4-PCD·CHB complex superimposed on a ribbon diagram of uncomplexed 3,4-PCD. The 6-fold averaged maps [$+5\sigma$ (blue) and -5σ (orange)] partially occlude the view of the active site iron and its ligands (yellow). (d) The PHB inhibitors (C and O atoms are shown as white and red sticks, respectively) bound in the 3-fold and active sites superimposed on the electrostatic isopotential contours calculated as in part b. The contours have been clipped just in front of the 1, 1, 1 ($+x$,$+y$,$+z$) 3-fold symmetry axis. The B and C protomers are labeled.

Scheme 1

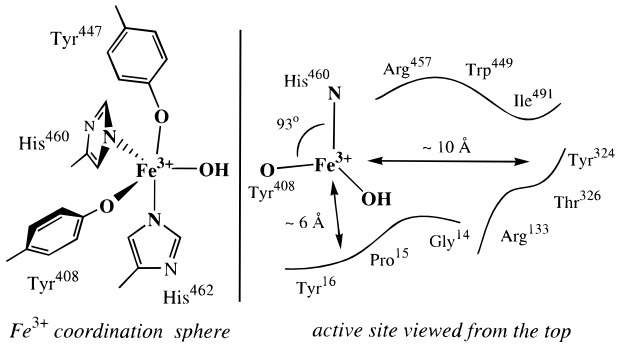

hydroxide ion (Felton et al., 1984; True et al., 1990), ligate the Fe^{3+} to yield approximate trigonal bipyramidal coordination geometry as illustrated in Scheme 1. There is a significant distortion of the iron coordination sphere toward octahedral geometry illustrated by the 93° $Tyr408^{O\eta}$−Fe^{3+}−$His460^{N\epsilon2}$ equatorial bond angle. A relatively open iron coordination face is also indicated by the 140° $His460^{N\epsilon2}$−Fe^{3+}−$Wat827^{OH}$ equatorial bond angle. Thus, if the iron coordination geometry were based only on the endogenous ligands, the coordination geometry would be octahedral with two open equatorial sites. These two sites are differentiated by their relationship to the active site cavity and the endogenous iron ligands. As seen from a view down the Fe^{3+}−$Tyr447^{O\eta}$ bond (Scheme 1), the coordination site opposite $His460^{N\epsilon2}$ (closest to Wat827) projects into an approximately 6 Å spherical cavity bordered by residues Ala13−Tyr16, Tyr408, Tyr447, His462, Trp400, and the iron. The second site, *trans* to $Tyr408^{O\eta}$, corresponds to the open coordination face in the uncomplexed 3,4-PCD structure and projects into a 10 Å × 6 Å elongated cavity bordered by residues Thr12−Pro15, Arg133, Tyr324, Thr326, Tyr447, Trp449, Arg457, Gln477, and Ile491. Both of these iron ligation sites are accessible to bulk solvent in the structure of the enzyme as isolated.

The interaction of substrates and inhibitors with 3,4-PCD has been investigated by numerous spectroscopic studies (see reviews referenced above). Resonance Raman spectroscopy [reviewed in Que (1989)] and EPR-detected superhyperfine broadening from ^{17}O-labeled substrates and solvent (Whittaker & Lipscomb, 1984b; Orville & Lipscomb, 1989, 1993) have been particularly effective in demonstrating that substrates, substrate-like inhibitors, and small molecules such

[3] The residue number also denotes the subunit chain (Ohlendorf et al., 1994); α-subunits are numbered from 1 to 200, and the *β*-subunits are numbered from 301 to 538. Ligands in the active site and 3-fold site are numbered 550 and 551, respectively; the iron is residue 600, and solvent numbering starts at 601.

Table 1: Selected Structural and Spectroscopic Parameters for the 3,4-PCD Complexes with Different Inhibitors

	none	IHB	MHP	PHP	MHB	PHB	CHB	FHB
phenolic pK_a[a]	−		9.9	9.9	9.9	9.3	7.5	7.8
inhibitor affinity[b] (K_i, μM)	−		∼10000	∼5000	4000	240	4	∼0.9
inhibitor surface area[c] (Å^2)	−	163	151	151	135	135	150	139
fraction exposed in active site	−	0.37	0.31	0.21	0.23	0.25	0.23	0.23
fraction exposed in 3-fold site	−	0.56	−	−	0.67	0.7	0.64	0.69
inhib^{O1}−Y324^{OH} distance (Å)	−	5.9	4.9	2.3	2.1	2.7	2.8	2.6
inhib^{C2}−G14$^{C\alpha}$ distance (Å)	−	4.5	4.7 (C6)	3.9	3.8	3.8	3.8	3.8
inhib^{C1}−P15$^{C\delta}$ distance (Å)	−	3.4	3.8	3.7	3.3	3.2	3.2	3.2
inhib^{C2}−I491$^{C\delta1}$ distance (Å)	−	4.9	3.3 (C6)	3.5	3.4	3.5	3.5	3.3
Fe^{3+} coord no.[d] (geometry)	5 (∼tbp)	5 (∼tbp)	5 (∼tbp)	5 (∼tbp)	4 (∼oct)	6 (∼oct)	6 (∼oct)	6 (∼oct)
optical absorption[e]								
λ_{max} (nm)	430−450	445 (635)	∼430	430 (∼600)	430−450	432	∼420	420
ϵ (mM^{-1} cm^{-1} per Fe^{3+})	2.9−3.2	3.8 (2.0)	∼3.5	4 (∼2)	2.9−3.2	3.4	∼3.5	3.6
resonance Raman shift[f]								
tyrosinate (cm^{-1})	1254, 1266	−	−	1256, 1288	1264	1262, 1289	1260, 1299	1263, 1303
inhibitor (cm^{-1})	−	−	−	1288	−	1276	1299	1303
EPR effects[g] ($S = 5/2$)								
E/D [D (cm^{-1})]	0.33 (1.6)	0.33	0.23	0.2	0.33	0.32, 0.24	0.3 (−1.7)	0.13, 0.21 (−1.8, −1.66)
^{17}O−solvent binding	yes	no	yes	no	no	yes	no	yes
^{17}O−inhibitor binding	−	−	yes	yes	no	yes	−	−

[a] From Smith and Martell (1989). [b] Data from Que et al. (1977), May et al. (1978), and May and Phillips (1979). [c] Calculated with a 1.4 Å probe radius for free inhibitor and inhibitor bound to protein excluding solvents. [d] Trigonal bipyramidal (tbp); octahedral (oct). [e] Data from May et al. (1978) and Que et al. (1977). [f] ν_{C-O} stretching modes from Felton et al. (1978), Siu et al. (1992), and Que and Epstein (1981) more accurately labeled as aromatic ring vibration modes (Michaud-Soret et al., 1996). [g] Data from Que et al. (1976), Whittaker and Lipscomb (1984), and Orville and Lipscomb (1989).

as CN^- bind directly to the iron. Moreover, these results demonstrate that at least two iron binding sites can be occupied by exogenous ligands and suggest that dynamic changes in the iron coordination sphere and/or changes in the orientation of the aromatic substrate are features of the catalytic cycle. Kinetic studies have shown that substrates bind to the enzyme through several steps and that subsequent oxygen activation and insertion chemistry also occur through several intermediates with quite different spectroscopic features (Bull & Ballou, 1981; Whittaker & Lipscomb, 1984a). These results also support significant perturbations in the interaction of substrate with the active site iron during catalysis that may be due to changes in orientation and/or the chemical nature of the substrate.

Together, the spectroscopic and kinetic results have been used to formulate structural models for the series of active site iron environments that are consistent with the proposed 3,4-PCD reaction cycle (Lipscomb & Orville, 1992). To date, these models are only supported by the crystallographic structure of the enzyme as it is isolated. The current report presents the crystal structures of seven competitive inhibitor complexes of 3,4-PCD and relates them to previous spectroscopic and kinetic results. This family of structures provides insights into the earliest stages of enzyme−substrate interactions leading to formation of the 3,4-PCD·substrate complex. The following paper extends these results with structures of anaerobic enzyme·substrate and enzyme·transition state analog complexes. Together, these reports describe three-dimensional models for several intermediates in the proposed 3,4-PCD reaction pathway and provide novel insights into the 3,4-PCD reaction mechanism and metalloenzyme catalysis in general.

MATERIALS AND METHODS

3,4-PCD was isolated from *P. putida*[2] (ATCC 23975) grown on *p*-hydroxybenzoate as the sole source of carbon and energy as previously described (Que et al., 1976). Enzyme assays were performed as previously described (Whittaker et al., 1990). Crystals of 3,4-PCD were grown aerobically at 4 °C by vapor diffusion as previously described (Ohlendorf et al., 1994). IHB, FHB, and CHB were gifts from P. Chapman. The phenolic pK_a for each inhibitor is reported in Table 1, and the binding affinity was based upon the reported inhibition or dissociation constants. Inhibitor stock solutions with concentrations equal to the final crystal soak concentration reported in Table 2 were made with mother liquor removed from the crystallization well; the pH was adjusted back to approximately 8.4 with 1 equiv of 8 N NaOH. The 3,4-PCD complexes were formed in a glass capillary by gradually replacing the mother liquor with the inhibitor stock solution in three steps (∼1:10, 1:1, final) followed by incubation at 23 °C for 5−24 h. The final concentration of the inhibitor (Table 2) in the crystal was at least 5 times greater than the reported K_i.

Each CuKα X-ray diffraction data set was collected from a single crystal at approximately 23 °C using a Siemens area detector mounted on a Rigaku RU-200 rotating anode with a 0.5 mm focal spot and a detector distance of 18 cm. The raw diffraction data were processed in the *C*2 unit cell using the XENGEN suite of programs (Howard et al., 1987). All reflections to a resolution limit where the mean $I/\sigma(I) = 1.0$ were retained and then reindexed to the equivalent *I*2 unit cell. The statistics from processing the X-ray diffraction data (Table 2) confirmed that the complexes were isomorphous to 3,4-PCD as isolated with only very small changes in the unit cell dimensions ($a = 196.52 \pm 0.68$ Å, $b = 127.32 \pm 0.49$ Å, $c = 134.15 \pm 0.53$ Å, and $\beta = 97.7 \pm 0.1°$). The refined phases and structure factors for the 3,4-PCD as isolated (*R*-factor of 0.172 for data between 5 and 2.15 Å; Ohlendorf et al., 1994) were used to calculate initial difference Fourier electron density maps of the form $(|F_{P\cdot I}| - |F_P|)e^{-i\alpha(P)}$, where $|F_{P\cdot I}|$ and $|F_P|$ are the structure factor amplitudes for the enzyme·inhibitor complex or the uncomplexed enzyme, respectively, and $\alpha(P)$ is the phase calculated for the refined atomic model for the 3,4-PCD structure. Since the asymmetric unit contained half the holoenzyme (six

Table 2: Summary of Data Collection and Atomic Model Refinement Statistics

data collection				
inhibitor (concentration)	MHB (50 mM)	PHB (50 mM)	MHP (50 mM)	PHP (50 mM)
resolution limit (Å)	2.2	2.0	2.1	2.0
*I*2 unit cell [*a*, *b*, *c* (Å)]	196.95, 127.56, 134.31	197.41, 127.97, 134.88	196.57, 127.77, 134.63	196.32, 127.12, 134.13
*I*2 unit cell β-angle (deg)	97.6	97.8	97.7	97.6
total observations (unique)	247,730 (132,191)	376,750 (156,351)	336,503 (161,694)	422,099 (189,802)
weighted R_{merge}^2 (absolute)[a]	0.0453 (0.060)	0.0520 (0.075)	0.0594 (0.087)	0.0647 (0.097)
$R_{isomorphous}$ to native[b]	0.152	0.174	0.176	0.17
fraction of data by shell	(10−2.2 Å) 0.782	(10−2.0 Å) 0.677	(10−2.1 Å) 0.798	(10−2.0 Å) 0.814
	(2.3−2.2 Å) 0.365	(2.1−2.0 Å) 0.322	(2.2−2.1 Å) 0.378	(2.1−2.0 Å) 0.347
average intensity [$I/\sigma(I)$]	(10−2.2 Å) 14.6	(10−2.0 Å) 11.1	(10−2.1 Å) 10.1	(10−2.0 Å) 8.2
model refinement				
reflections ($F > 1.0\sigma$)[c]	110 643	130 625	130 591	147 999
final *R*-factor[d]	(6.0−2.2 Å) 0.159	(6.0−2.0 Å) 0.163	(6.0−2.1 Å) 0.169	(6.0−2.0 Å) 0.175
	(2.4−2.2 Å) 0.211	(2.2−2.0 Å) 0.218	(2.2−2.1 Å) 0.227	(2.2−2.0 Å) 0.247
rms deviation from ideal				
23 symmetry (Å)	0.173	0.177	0.174	0.176
bond distances (Å) (no.)	0.021 (21 180)	0.022 (21 180)	0.021 (21 126)	0.021 (21 126)
bond angles (deg)	2.9	2.9	2.9	2.9
number of non-H protein atoms	20 616	20 616	20 562	20 562
number of solvent O atoms	1416	1446	1446	1434
inhibitors per asymmetric unit	12	12	6	6
mean *B* values (Å^2)				
α-subunit, β-subunit, solvent	27.0, 21.1, 22.4	25.8, 19.8, 21.4	27.7, 21.6, 22.7	24.6, 17.8, 19.5
inhibitors	26.2 (32.1[e])	20.1 (24.0[e])	24.7	19.6

data collection			
inhibitor (concentration)	FHB (50 mM)	CHB (35 mM)	IHB (125 mM)
resolution limit (Å)	2.2	2.1	2.2
*I*2 unit cell [*a*, *b*, *c* (Å)]	196.03, 127.22, 133.70	195.39, 126.52, 133.33	197.00, 127.07, 134.08
*I*2 unit cell β-angle (deg)	97.7	97.8	97.5
total observations (unique)	469 264 (167 067)	321 914 (150 935)	269 229 (163 414)
weighted R_{merge}^2 (absolute)[a]	0.0639 (0.102)	0.0503 (0.068)	0.0479 (0.055)
$R_{isomorphous}$ to native[b]	0.206	0.168	0.183
fraction of data by shell	(10−2.2 Å) 0.933	(10−2.1 Å) 0.752	(10−2.2 Å) 0.828
	(2.3−2.2 Å) 0.826	(2.2−2.1 Å) 0.393	(2.4−2.2 Å) 0.429
average intensity [$I/\sigma(I)$]	(10−2.2 Å) 9.4	(10−2.1 Å) 11.8	(10−2.2 Å) 14.3
model refinement			
reflections ($F > 1.0\sigma$)[c]	125 979	121 498	113 850
final *R*-factor[d]	(6.0−2.2 Å) 0.179	(6.0−2.1 Å) 0.167	(6.0−2.2 Å) 0.159
	(2.3−2.2 Å) 0.236	(2.2−2.1 Å) 0.212	(2.3−2.2 Å) 0.212
rms deviation from ideal			
23 symmetry (Å)	0.168	0.175	0.155
bond distances (Å) (no.)	0.023 (21 192)	0.023 (21 192)	0.020 (21 192)
bond angles (deg)	3.0	3.0	2.8
number of non-H protein atoms	20 628	20 628	20 628
number of solvent O atoms	1452	1452	1476
inhibitors per asymmetric unit	12	12	12
mean *B* values (Å^2)			
α-subunit, β-subunit, solvent	25.8, 19.4, 21.0	25.1, 18.3, 19.9	26.6, 20.0, 21.6
inhibitors	18.8 (24.2[e])	20.5 (22.6[e])	25.9 (18.5[e])

[a] Weighted $R_{merge} = [\sum_{hkl}\sum_i[(I_i - \langle I\rangle_i G_i)/\sigma_i]^2/\sum_{hkl}\sum_i(I_i/\sigma_i)^2]^{1/2}$; absolute $R_{merge} = \sum_{hkl}\sum_i|I_i - \langle I\rangle_i G_i|/\sum_{hkl}\sum_i I_i$, where, for observation *i* of reflection *hkl*, I_i is the observed intensity, $\langle I\rangle_i$ is its mean intensity, G_i is the scaling function applied, and σ_i is the standard deviation. [b] $R_{isomorphous} = \sum_{hkl}|F_{P\cdot I} - F_P|/\sum_{hkl}F_P$, where $F_{P\cdot I}$ and F_P are the structure factors for the 3,4-PCD·inhibitor complexes and 3,4-PCD as isolated, respectively. [c] Reflections between 6.0 Å and the resolution limit. [d] *R*-factor $= \sum_{hkl}|F_o - F_c|/\sum_{hkl}F_c$, where F_o and F_c are the observed and calculated structure factors, respectively. [e] Ligands in 3-fold binding site.

protomers), 6-fold averaged electron density maps were calculated and superimposed upon protomer A of 3,4-PCD using AVERAGE6 (D. H. Ohlendorf). This program was specifically written to average the electron density for 3,4-PCD starting with maps calculated on a 0.5 Å grid and producing a final map on a 0.9 Å grid covering protomer A. Before averaging, the correlation coefficient between the $2|F_o| - |F_c|$ electron density of each monomer was typically 0.8 or higher. The averaged electron density maps were cleaner than the unaveraged maps since the averaging reduced the errors associated with incomplete and/or weak diffraction data in the highest-resolution shells. The other five protomers were also inspected with respect to the unaveraged electron density maps or rotated onto protomer A using the noncrystallographic symmetry transformations and examined with respect to the averaged electron density maps. Atomic models of the competitive inhibitors were built and energy minimized using Discover from the InsightII (Biosym Corp., La Jolla, CA) software package.

PROTIN/PROLSQ (Hendrickson & Konnert, 1980; Hendrickson, 1985) was used to refine the models of the 3,4-PCD complexes between 6 Å and the resolution limit of the diffraction data using reflections with an F of $\geq 1\sigma$ on Cray Y-MP and C-90 supercomputers as described previously (Ohlendorf et al., 1994). During refinement, the idealized hydroxyphenylacetates were restrained to two planes while the hydroxybenzoate derivatives were restrained to one plane over all atoms. Atoms of the inhibitors are named according to standard nomenclature with the exception of the carboxylate groups (atoms C7, O1, and O2, where O1 is on the same side of the ring as the C2−C3 bond) and the acetate groups (atoms C7, C8, O1, and O2, where C7 is the methylene CH_2

group). The phenolic oxygen atoms of tyrosine residues in the neutral or ionized state are indicated with OH and Oη atom names, respectively. Protonated and ionic phenolate groups on the inhibitors are indicated by OH3 (or OH4) and O3 (or O4) atom labels, respectively. The starting models consisted of the refined 3,4-PCD structure from which the active site solvent molecules had been removed. The inhibitor was placed in the 6-fold averaged $|F_{P\cdot I}| - |F_P|$ and $2|F_{P\cdot I}| - |F_P|$ electron density within the active site of protomer A (and at the 3-fold binding site if indicated) followed by real space refinement with respect to the $2|F_{P\cdot I}| - |F_P|$ electron density. The coordinates for the ligands within the other five protomers in the asymmetric unit were obtained from noncrystallographic symmetry transformations of the protomer A coordinates. The *R*-factors for the starting models ranged from 0.207 to 0.275 and refined to values between 0.159 and 0.179. The final models have an estimated error of 0.25 Å in bond distances and approximately 3° in bond angles (Table 2). Solvent molecules bound to the iron were added in the last stages of the refinement as indicated by an at least $+5\sigma$ $|F_o| - |F_c|$ averaged density. Residues were numbered according to Ohlendorf et al. (1994). All the enzyme·inhibitor complexes have one side chain modification per protomer at Cys429 (not shown). An extra lobe of positive electron difference density projects from the Cys429 Sγ atom and could not be modeled adequately with solvent molecules. However, the density was accommodated very well by a β-mercaptoethanol molecule linked via a disulfide bond to the Sγ of the Cys429 which was included in the final 10−15 cycles of refinement for each complex.

The MidasPlus suite of programs (Ferrin et al., 1988) from the Computer Graphics Laboratory of the University of California at San Francisco (supported by NIH Grant RR-01081) was used to calculate solvent accessibility (1.4 Å radius probe sphere) and secondary structure and to prepare Figures 1a,c and 6. Electrostatic potential calculations were performed with GRASP (Honig & Nicholls, 1995; Gilson et al., 1988) using standard potentials for protein residues and inhibitors in 0.1 M salt. The iron atom was assigned either a +0.5 or 0 charge in the uncomplexed 3,4-PCD or the inhibitor complexes, respectively. These values were deduced by observing that the two tyrosinate Fe^{3+} ligands and the partially occupied solvent (Wat827, hydroxide) in the uncomplexed 3,4-PCD structure yield partial charge neutrality, while a fully occupied inhibitor phenolate yields full charge neutrality of the metal center. Procheck (Laskowski et al., 1993) was used to assess the stereochemical quality of the models. Electron density map formats were interconverted using the CCP4 suite of programs. Figures 2, 3a, 4, and 5 were prepared with MOLSCRIPT (Karulis, 1991). Model building was performed with the graphics program TOM (Jones, 1978) on Silicon Graphics workstations.

RESULTS

General Structural Features. 3,4-PCD binds negatively charged substrates and inhibitors despite the fact that the holoenzyme carries a strong negative charge above neutral pH. Indeed, electrostatic calculations of 3,4-PCD in 0.1 M salt yield very large −1 kT isopotential contour surfaces projecting from the α-subunits and portions of the β-subunits around the 3-fold symmetry axes (Figure 1b). The only +1 kT isopotential contour surfaces visible on the outside of the holoenzyme project from the active site within each protomer (Figure 1b). This is derived from the local regions of positive potential emanating from seven arginines (Arg64, Arg133, Arg330, Arg407, Arg409, Arg414, and Arg450) and two lysines (Lys325 and Lys411) surrounding the active sites. Only three acidic residues (Asp65, Asp413, and Glu162) are within the same volume, and two (Glu162 and Asp65) are involved in ionic interactions with Arg133 and/or Arg330. Therefore, 3,4-PCD appears to attract its negatively charged substrates and inhibitors into very localized, positively charged regions around the exterior of each active site. This is similar to the electrostatic attraction of superoxide to the active site of Cu,Zn superoxide dismutase (Getzoff et al., 1992; Fisher et al., 1994).

The presence of each inhibitor within the catalytic active site was easily seen in the $|F_{P\cdot I}| - |F_P|$ Fourier difference maps calculated for each 3,4-PCD complex examined here. However, they were particularly clear in the halogenated hydroxybenzoate complexes due to the intense difference features centered on the halide (Figure 1c). For example, the iodine atom in the active site of the 3,4-PCD·IHB complex produced $+40\sigma$ and $+12\sigma$ features in the averaged and unaveraged difference Fourier maps, respectively.

The inhibitor complex structures also revealed an unexpected[4] set of secondary binding sites for inhibitors (and substrates) clustered around the apical ends of the 3-fold symmetry axes between the A, B, and C and D, E, and F protomers. The three $+80\sigma$ (averaged) or $+18\sigma$ $|F_{P\cdot I}| - |F_P|$ (unaveraged) difference features near the 3-fold symmetry axes of the 3,4-PCD·IHB complex were the strongest features observed in any of the initial difference Fourier maps. All of the benzoate·inhibitor complexes (and the anaerobic PCA complex described in the following paper) showed binding to these secondary sites. The affinity of the inhibitors for these binding sites appears to be based upon complementary shape and charge (Figures 1d and 2). For example, the aromatic portion of each inhibitor makes hydrophobic interactions with the side chains of Leu320, Pro322, and Ile328 from adjacent protomers and provides the only solvent-excluded surface area on these ligands (Table 1). One hydrogen bond between each inhibitor C4-phenol group and $Arg333^O$ is observed, and electrostatic stabilization is suggested by the proximity of the carboxylate moiety of each inhibitor to the amino group of Lys318 (less than 5 Å separation). Three approximately 25 Å long channels with positive electrostatic potential (Figure 1d) connect the secondary binding sites to the active sites in the 3-fold related protomers.

Although the protomeric rms positional differences for the main chain atoms in uncomplexed 3,4-PCD and the 3,4-PCD·inhibitor complexes are typically only about 0.4 Å, the enzyme·inhibitor complexes do have one significant structural alteration outside the active site. The $|F_{P\cdot I}| - |F_P|$ difference maps (Figure 1c) indicate a conformational change in the α-subunits around α-helix B (residues 22−27) and the loop connecting β-strands 3 and 4 (residues 98−103). These two adjacent regions are approximately 15−20 Å from the Fe^{3+} on the exterior surface of the active site and yield

[4] A 50 mM IHB soak of 3,4-PCD was investigated during the search for isomorphous heavy metal derivatives, and the difference Patterson maps revealed a binding site very near the 3-fold symmetry axis (D. H. Ohlendorf, unpublished observation). However, since the IHB was expected to bind specifically within the active site, the derivative was excluded from the MIR solution of the uncomplexed 3,4-PCD structure.

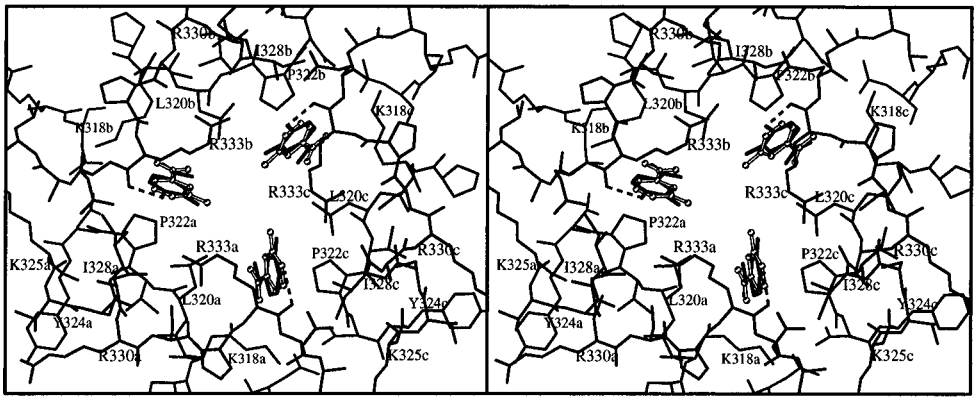

FIGURE 2: Divergent stereoview of the 3-fold binding site in the 3,4-PCD·inhibitor complexes. A superposition of the FHB (black) and MHB (white) complexes with all the protein residues between Lys318 and Ala335 shown for the A protomer (a), B protomer (b), and C protomer (c) of the 3,4-PCD·FHB complex.

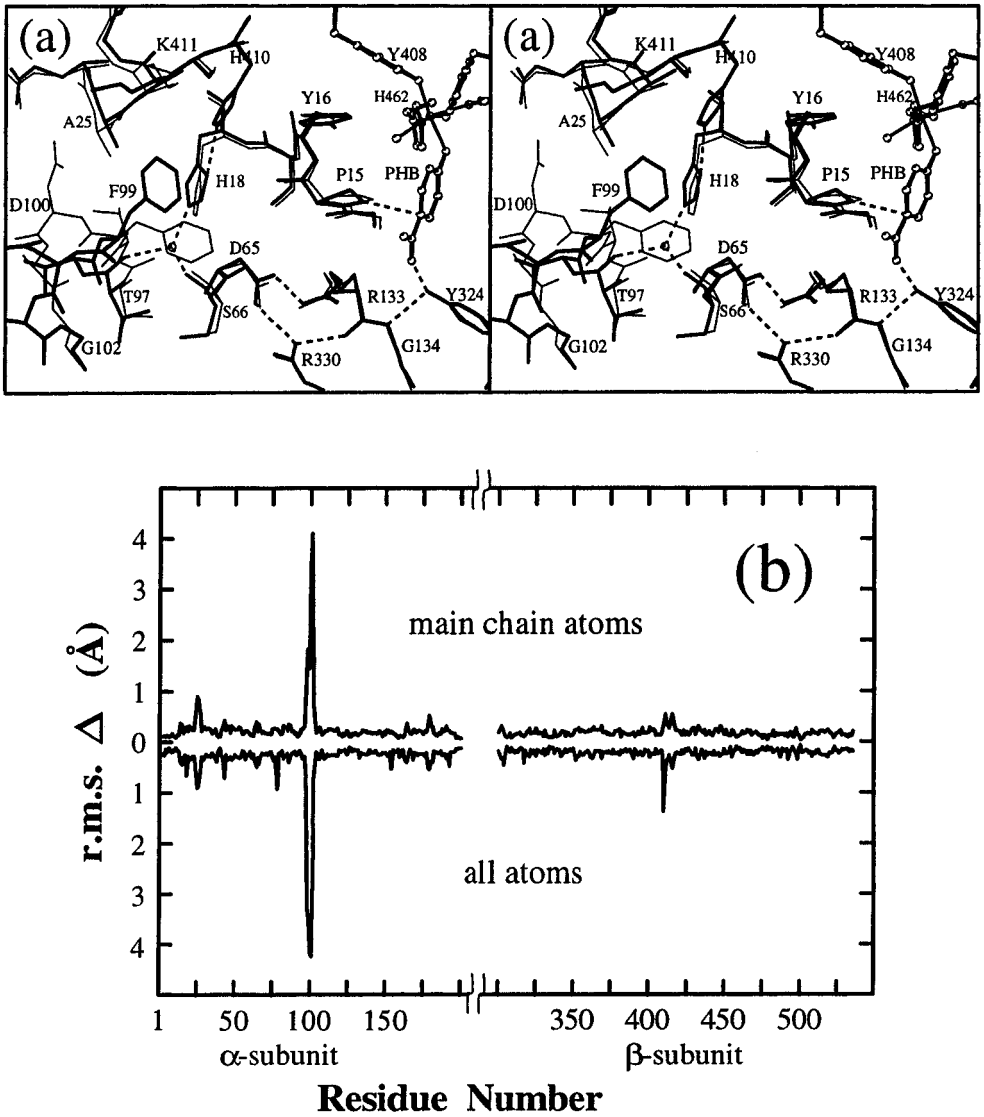

FIGURE 3: Regions of the refined enzyme·inhibitor structures with the largest differences compared to the enzyme as isolated. (a) A divergent stereoview highlighting the region with the largest structural difference between the 3,4-PCD·PHB complex (thick lines) and uncomplexed structure (thin lines). Dashed lines indicate hydrogen bonds in the 3,4-PCD·PHB complex, except for the dashed line between Pro15$^{C\delta}$ and PHB^{C1} which indicates a close van der Waals contact. (b) The rms position differences for the 3,4-PCD·PHB complex compared to the uncomplexed 3,4-PCD structure. The top and lower portions show the differences averaged over the main chain atoms or all atoms, respectively.

the largest positional differences between the uncomplexed 3,4-PCD structure and any of the inhibitor complexes (Figure 3b). Figure 3a shows the final refined atomic model for the 3,4-PCD·PHB complex in this region superimposed on the structure of 3,4-PCD as isolated. The thermal factors for the atoms in the loop between residues 97 and 102 range from 30−45 Å^2 and are among the highest in the models, suggesting flexibility in this region. The positional shifts originating at Pro15, which makes van der Waals contact with each inhibitor, are shown in Figure 3a. Together, these conformational changes, which are also observed in the 3,4-PCD·PCA complex (Orville et al., 1997), enlarge the opening

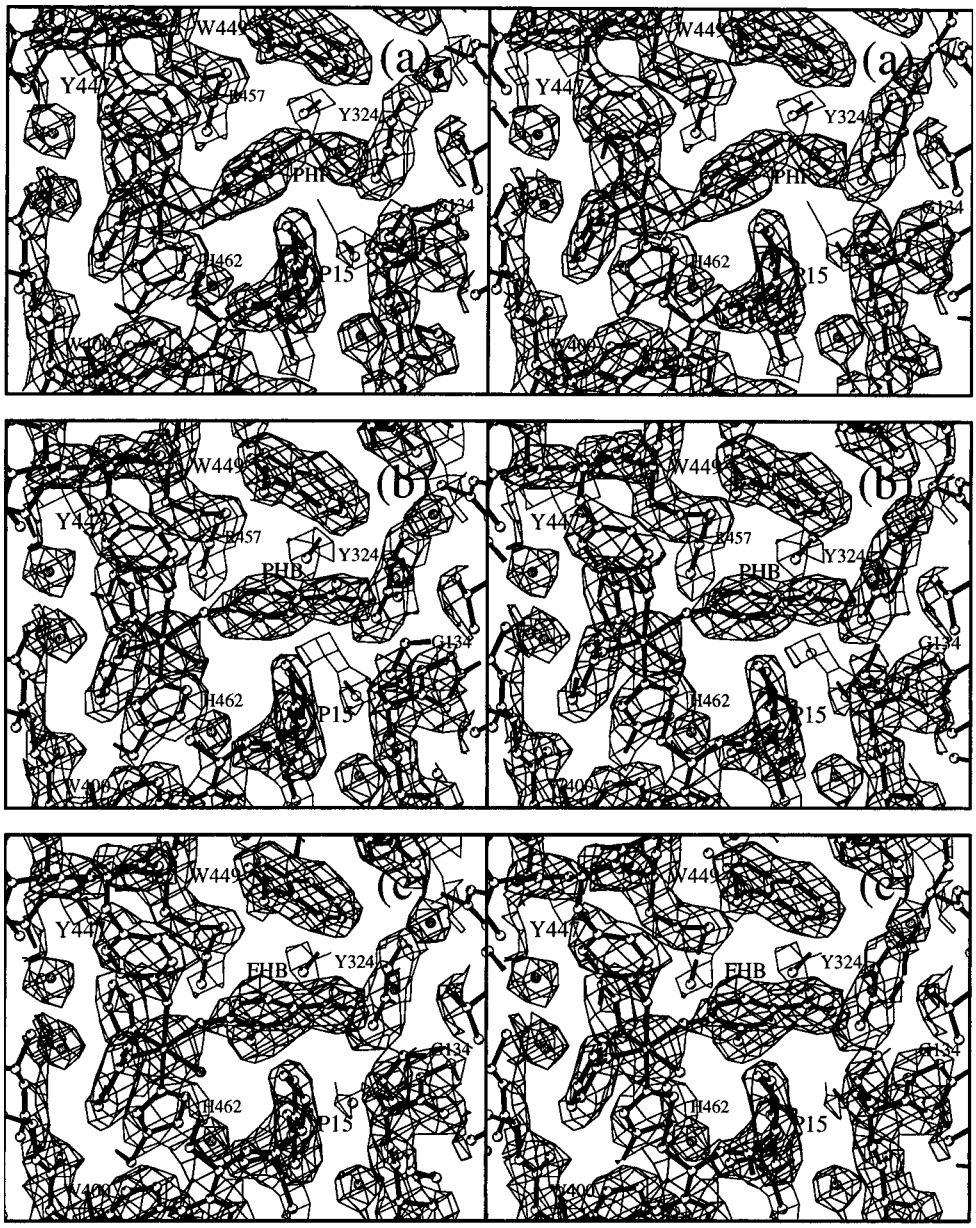

FIGURE 4: Divergent stereoviews of the final averaged $2|F_o| - |F_c|$ electron density maps contoured at 1.5σ in the active site region. (a, top) The Fourier map for the 3,4-PCD·PHP complex calculated at 2.0 Å resolution with its refined atomic model superimposed. (b, middle) The map calculated at 2.0 Å resolution for the 3,4-PCD·PHB complex and the atomic model. (c, bottom) The map for the 3,4-PCD·FHB complex calculated at 2.2 Å resolution superimposed on its refined atomic model. Prepared with MINIMAGE (Arnez, 1994) and MOLSCRIPT (Kraulis, 1991).

of the active site cavity and may have a functional role by increasing the dioxygen accessibility and/or product dissociation rate.

Protein−Inhibitor Interactions within the Active Site. Incubation of 3,4-PCD crystals with each inhibitor produced a subtle but distinct color change in accord with previous solution studies (Table 1). The $|F_{P\cdot I}| - |F_P|$ difference maps from all the complexes clearly indicate that the inhibitors bind very near the iron and that the five coplanar solvent molecules and Wat827 observed in the active site structure of 3,4-PCD as isolated were either displaced or shifted into a different binding site. The quality of the final electron density maps in the active site region is very good as demonstrated in Figure 4 with the 3,4-PCD·PHP, 3,4-PCD·PHB, and 3,4-PCD·FHB complexes. These maps are typical of those observed for each inhibitor and unambiguously establish the position of the inhibitors within the 3,4-PCD catalytic site. For example, the electron density for the PHP molecule clearly indicates a bend at the methylene carbon of the acetate group (Figure 4a). In contrast, the density for the PHB·inhibitor reveals two planar lobes corresponding to the aromatic ring and the carboxylate group (Figure 4b). The position of the fluorine group is clearly indicated in the electron density for the FHB·inhibitor complex (Figure 4c). Thus, the electron density maps easily differentiate the inhibitor complexes despite the similarity of the inhibitor molecules used in this study.

The active site of protomer A from uncomplexed 3,4-PCD and the inhibitor complexes are presented in Figure 5. The structures show hydrophilic interactions with the inhibitors through residues Arg133, Tyr324, Thr326, Arg457, and Gln477 and hydrophobic interactions via Gly14, Pro15, Trp449, and Ile491. Together, these residues form a narrow crevasse in which the hydrophobic residues partition the hydrophilic residues with Arg133, Tyr324, and Thr326 at the back and Arg457, Gln477, and the iron at the front. This creates an active site microenvironment that complements the chemical features of the inhibitors (and

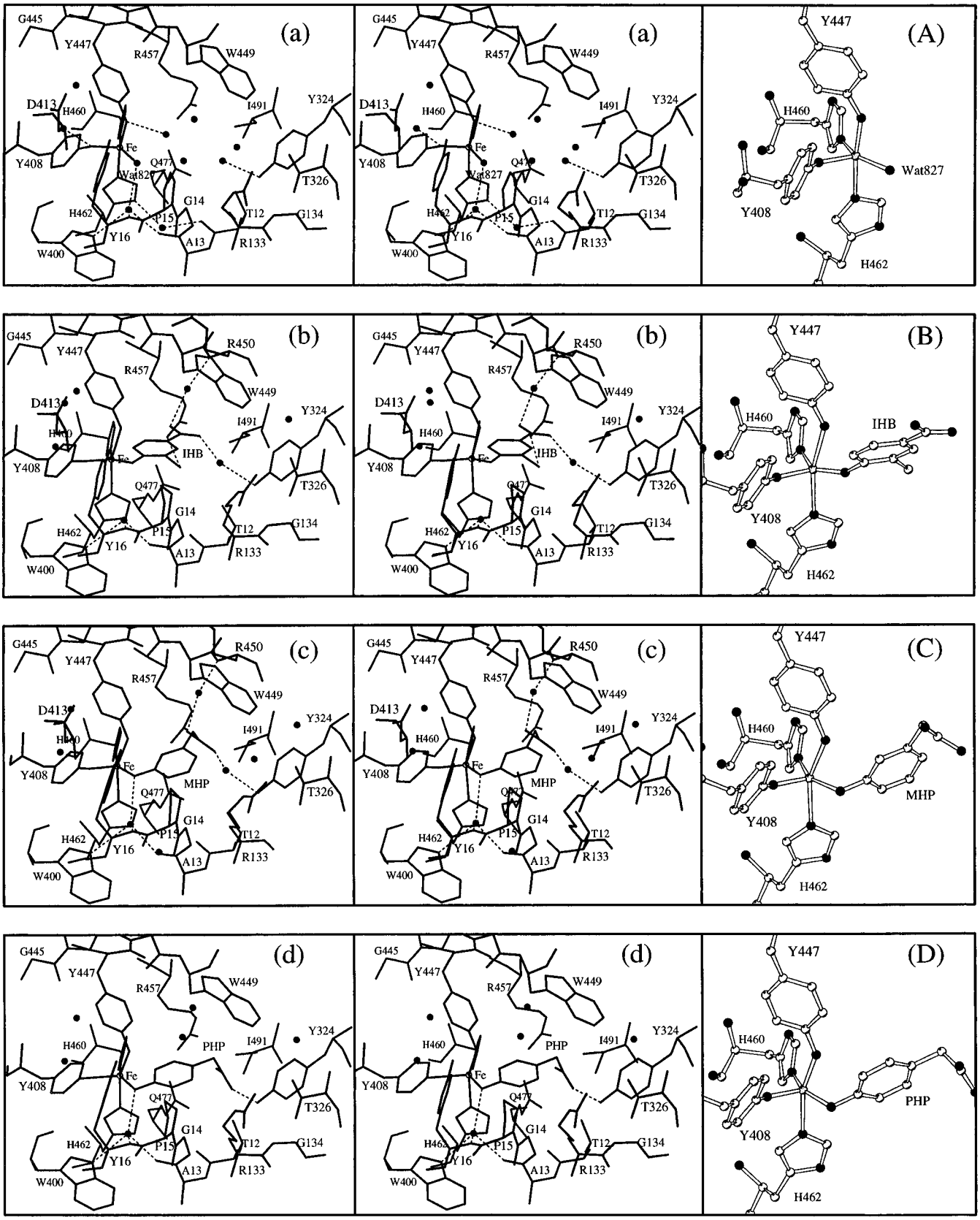

FIGURE 5: Divergent stereoviews of the final models for the 3,4-PCD·ligand complexes arranged in order of increasing ligand affinity. Each structure shows all the first-shell residues of the active site within approximately 6 Å of the ligand. Proposed bonds between the Fe^{3+} and coordinating atoms from either the endogenous or exogenous ligands are drawn as solid lines, while proposed hydrogen bond interactions

substrates). All the inhibitors, with the exception of MHB, coordinate the Fe^{3+} through their phenolate moiety rather than through their carboxylate or acetate groups. The acetate or carboxylate groups form an electrostatic interaction with $Arg133^{N\epsilon}$ and form a strong hydrogen bond with $Tyr324^{OH}$.

The inhibitors utilized in this study have inhibition constants that range over 4 orders of magnitude (Table 1). Comparison of the structures (Figure 5a−h) reveals that the number and strength of hydrogen bonds, as well as the inhibitor solvent-exposed surface area, correlate with relative affinity. For example, the two weakest binding inhibitors,

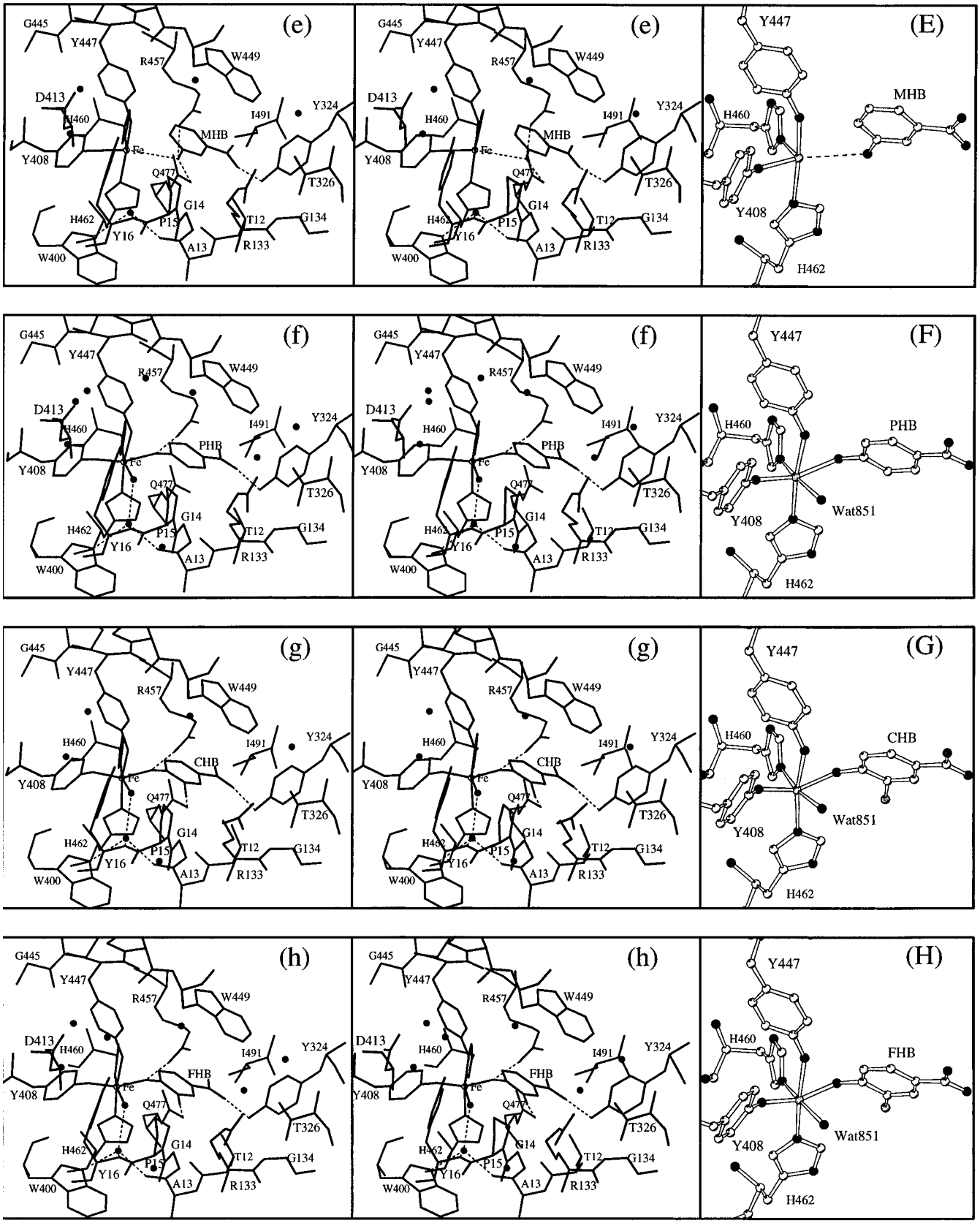

are indicated with dashed lines: (a) uncomplexed 3,4-PCD (Ohlendorf et al., 1994), (b) 3,4-PCD·IHB complex, (c) 3,4-PCD·MHP complex, (d) 3,4-PCD·PHP complex, (e) 3,4-PCD·MHB complex, (f) 3,4-PCD·PHB complex, (g) 3,4-PCD·CHB complex, and (h) 3,4-PCD·FHB complex. (A−H) A comparison of the Fe^{3+} coordination geometry observed for the uncomplexed and inhibitor complexes of 3,4-PCD.

IHB and MHP (Figure 5b,c), utilize solvent molecules to mediate long hydrogen bond interactions between $Arg450^{N}$ and $Tyr324^{OH}$ and their respective carboxylate or acetate groups. In contrast, the highest-affinity inhibitors, CHB and FHB (Figure 5g,h), form complexes with short hydrogen bonds directly between their O1 atom and $Tyr324^{OH}$. In addition, an electrostatic interaction between the inhibitor O2 atom and $Arg133^{N\epsilon}$ may help neutralize the negative charge of these inhibitors. The higher-affinity inhibitors also generally fit in the active site better and consequently minimize the solvent accessible surface area (Table 1) relative to the lower-affinity inhibitors. For example, the

Table 3: Average Bond Distances and Angles for the Six Active Site Fe^{3+} Centers per Asymmetric Unit

	none[a]	IHB	MHP	PHP	MHB	PHB	CHB	FHB
$Y408^{O\eta}$−Fe distance (Å)[b]	1.8	1.8	1.8	1.8	1.8	1.9	1.8	1.8
$Y447^{O\eta}$−Fe distance (Å)[b]	1.9	2.1	2.0	1.9	2.1	2.1	2.2	2.1
$H460^{N\epsilon 2}$−Fe distance (Å)[b]	2.3	2.2	2.2	2.2	2.3	2.3	2.2	2.3
$H462^{N\epsilon 2}$−Fe distance (Å)[b]	2.3	2.3	2.3	2.3	2.3	2.2	2.2	2.2
$inhib^{Ox}$−Fe distance (Å)[b]	−	1.6	1.9	1.8	(3.4)[c]	2.2	2.1	2.0
solvent−Fe distance (Å)[b]	1.9	−	−	−	−	2.1	2.1	2.3
Fe−$inhib^{Ox}$−$inhib^{Cx}$ [e] angle (deg)[d]	−	146	112	119	(96)[c]	137	145	137
$Y408^{O\eta}$−Fe−$Y447^{O\eta}$ angle (deg)[d]	99	97	102	103	94	88	77	85
$Y408^{O\eta}$−Fe−$H460^{N\epsilon 2}$ angle (deg)[d]	93	98	97	103	94	92	91	88
$Y408^{O\eta}$−Fe−$H462^{N\epsilon 2}$ angle (deg)[d]	91	98	91	97	92	102	111	104
$Y408^{O\eta}$−Fe−$inhib^{Ox}$ angle (deg)[d]	−	131	115	119	(171)[c]	152	135	148
$Y408^{O\eta}$−Fe−solvent angle (deg)[d]	124	−	−	−	−	105	105	107
$Y447^{O\eta}$−Fe−$H460^{N\epsilon 2}$ angle (deg)[d]	94	88	90	90	87	88	89	86
$Y447^{O\eta}$−Fe−$H462^{N\epsilon 2}$ angle (deg)[d]	167	165	166	160	169	168	169	167
$Y447^{O\eta}$−Fe−$inhib^{Ox}$ angle (deg)[d]	−	74	84	92	(90)[c]	65	59	63
$Y447^{O\eta}$−Fe−solvent angle (deg)[d]	93	−	−	−	−	95	94	100
$H460^{N\epsilon 2}$−Fe−$H462^{N\epsilon 2}$ angle (deg)[d]	79	89	90	87	87	84	87	84
$H460^{N\epsilon 2}$−Fe−$inhib^{Ox}$ angle (deg)[d]	−	126	146	136	(91)[c]	86	94	87
$H460^{N\epsilon 2}$−Fe−solvent angle (deg)[d]	141	−	−	−	−	162	162	163
$H462^{N\epsilon 2}$−Fe−$inhib^{Ox}$ angle (deg)[d]	−	96	88	76	(84)[c]	105	112	108
$H462^{N\epsilon 2}$−Fe−solvent angle (deg)[d]	87	−	−	−	−	89	87	87
$inhib^{Ox}$−Fe−solvent angle (deg)[d]	−	−	−	−	−	79	73	82

[a] From Ohlendorf et al. (1994). [b] Estimated errors in bond distances are ±0.3 Å. [c] The distance between the Fe^{3+} and OH of MHB is too long to be considered a bond. [d] Estimated errors in bond angles are ±3°. [e] The $inhib^{Cx}$ atom is either the C1 or C6 atom in *p*-hydroxy- or *m*-hydroxy-containing inhibitors, respectively.

structures of the 3-halo-4-hydroxybenzoate inhibitor complexes (Figure 5b,g,h) clearly show that CHB and FHB fill the narrowest portion of the active site cavity between Gly14, Pro15, Trp449, and Ile491 better than IHB. This reduces the solvent-exposed surface area of CHB and FHB by about 40% relative to that of IHB. Moreover, in the high-affinity binding orientation, substituents at C3 and/or C4 in CHB, FHB, PHB, and MHB form hydrogen bonds with $Arg457^{N\eta 1}$ and $Gln477^{N\epsilon 2}$ near the front of the active site cavity, while the low-affinity complexes do not. Finally, the rotational freedom present in the methylene group of PHP allows for hydrophobic and hydrogen bond interactions with active site residues that are very similar to those of the PHB complex (Figure 5d,f). However, the PHP^{O4} atom coordinates the iron to yield trigonal bipyramidal coordination geometry, whereas the PHB^{O4} atom binds the iron from a site *trans* to $Tyr408^{O\eta}$ and yields octahedral geometry.

Variability of the Iron Coordination Geometry in the 3,4-PCD·Inhibitor Complexes. The ligands to the Fe^{3+} are shown in Figure 5A−H and highlight the coordination geometry for the inhibitor complexes. The iron to ligand bond distances and angles averaged from the six independent active sites per asymmetric unit are listed in Table 3. These bond distances and coordination geometries were not restrained during the refinement, and the final results are similar to metal−ligand bond distances and the coordination geometry determined from other metalloproteins (Howard & Rees, 1991; Glusker, 1991). The four endogenous iron ligands in all the complexes are essentially unperturbed relative to the uncomplexed 3,4-PCD structure. However, the different binding orientations of the inhibitors yield the following iron coordination geometries: (i) four-coordinate, octahedral with no exogenous ligands (Figure 5E); (ii) five-coordinate, trigonal bipyramidal with one exogenous ligand (Figure 5B−D); and (iii) six-coordinate, octahedral with two exogenous ligands (Figure 5F−H). In each case, however, the observed geometry is slightly distorted from ideal.

The three lowest-affinity ligands (IHB, MHP, and PHP) yield approximate trigonal bipyramidal iron geometry that is similar to the iron coordination environment in the uncomplexed enzyme. Indeed, examination of the average bond distances and angles in Table 3 suggests that Wat827 from the uncomplexed enzyme nearly superimposes with the phenolate group of these inhibitors. However, the bond angles between the inhibitor phenolate atom, the Fe^{3+}, and the equatorial endogenous Fe^{3+} ligands range from 115 to 146° and indicate distortion in the trigonal bipyramidal geometry.

Each of the other inhibitor complexes yields essentially octahedral iron coordination geometry. In the PHB, CHB, and FHB complexes, the C4-phenolate group coordinates the iron from a site *trans* to $Tyr408^{O\eta}$ (Figure 5F−H). The electron density maps (Figure 4) for these complexes also indicate that a solvent molecule occupies the adjacent equatorial site. Thus, the resulting octahedral iron coordination geometry for these complexes includes two exogenous ligands. In contrast, the 3,4-PCD·MHB complex yields a more highly distorted coordination sphere. This structure shows that the MHB^{OH3} group is located 3.4 Å away from the iron, out of bonding distance, and forms hydrogen bonds with $Arg457^{N\eta 1}$ and $Gln477^{N\epsilon 2}$ (see Figure 5e). Several trial models were refined for the 3,4-PCD·MHB complex to test for solvent coordination in the ligand site *trans* to $His460^{N\epsilon 2}$. However, these trials always yielded insufficient $2|F_o| - |F_c|$ density and negative $|F_o| - |F_c|$ density over the solvent atom in this coordination site. Therefore, the iron in the 3,4-PCD·MHB complex appears to have only four endogenous protein ligands. On the other hand, the coordination bond angles for these ligands are closer to ideal octahedral geometry than observed for the PHB, CHB, or FHB complexes.

Several hydrogen bonds to the atoms or residues coordinating the iron may influence the iron ligation geometry and, perhaps, stabilize the inhibitor complexes. $Tyr408^{O\eta}$ accepts a hydrogen bond from a solvent molecule (Wat643) in a buried cavity behind the metal in all the complexes, whereas $Tyr447^{O\eta}$ does not accept any hydrogen bonds in any complex. The $His460^{N\epsilon 2}$ and $His462^{N\epsilon 2}$ atoms ligate the iron

and, therefore, cannot participate in additional hydrogen bonds. However, $His462^{N\delta 1}$ forms a hydrogen bond with a solvent molecule (Wat605) on the floor of the active site cavity in each complex. A hydrogen bond between the phenolate group of either MHP or PHP and a buried solvent molecule (Wat606 between $Trp400^{N\epsilon 1}$, $Tyr16^{N}$, and $Ala13^{O}$) may help stabilize the trigonal bipyramidal geometry for these complexes. Similarly, hydrogen bonds between the C4-phenolate group of either PHB, CHB, or FHB and $Arg457^{N\eta 1}$ probably help stabilize the octahedral metal geometry of these complexes.

A potentially significant distortion of the iron coordination sphere in the PHB, CHB, and FHB complexes is apparent in the $Fe^{3+}-Tyr447^{O\eta}$ bond (Table 3). The acute $Tyr447^{O\eta}-Fe^{3+}-inhibitor^{O4}$ and obtuse $His462^{N\epsilon 2}-Fe^{3+}-inhibitor^{O4}$ bond angles indicate that the C4-phenolate from these inhibitors is slightly above the plane of the equatorial ligands. This appears to result from the cumulative protein−inhibitor interactions and, in particular, the $inhibitor^{O1}\cdots Tyr324^{OH}$ hydrogen bond. The distortion of the iron coordination sphere observed in these complexes may have functional consequences because the following paper shows that substrate chelation occurs concomitantly with $Tyr447^{OH}$ dissociation. The $Fe^{3+}-Tyr447^{O\eta}$ bond in these inhibitor complexes is probably strained relative to those of the other endogenous iron ligands, making it more susceptible to dissociation. Moreover, Tyr447 is the only iron ligand with any significant solvent-exposed surface area in the uncomplexed enzyme. Consequently, Tyr447 has the unique potential to rotate into another orientation without requiring numerous additional side chain reorientations.

DISCUSSION

This is the first of several reports that use X-ray crystallography to probe the proposed reaction mechanism of 3,4-PCD by examining the structures of diagnostic inhibitor and substrate complexes. With the exception of MHB, the phenolate group of each inhibitor binds to the active site iron in accord with all the previous spectroscopic results. However, these structures show at least three fundamentally different orientations of inhibitors in the active site: (i) inhibitors that protrude out of the active site cavity but still coordinate the iron to yield trigonal bipyramidal coordination geometry (e.g. IHB and MHP), (ii) ligand binding within the active site that is sufficient to dissociate the active site solvent molecules but without direct coordination to the iron (e.g. MHB), and (iii) inhibitors that bind completely within the active site, directly coordinate the iron, and yield octahedral geometry (e.g. PHB, CHB, and FHB). As will be demonstrated in the following report (Orville et al., 1997), substrate binding defines yet another orientation. This level of complexity is unexpected for an enzyme like 3,4-PCD that shows essentially 100% specificity in the site of aromatic ring cleavage. However, these results are consistent with our previous studies that indicate different binding modes for different inhibitors, heterogeneity in the solution enzyme·substrate complex, and a mechanistic rationale for changes in substrate binding orientation during catalysis [reviewed in Lipscomb and Orville (1992)]. These and other aspects of this study will be discussed in the context of previous results in the following sections.

Correlation of the 3,4-PCD·Inhibitor Structures to Previous Kinetic and Spectroscopic Data. The crystal structures reported here are remarkably consistent with nearly all the previous kinetic and spectroscopic results as summarized in Table 1. Several early studies reported the steady state kinetic parameters of competitive inhibitors of 3,4-PCD in an effort to define which functional groups of PCA most affect binding affinity (Que et al., 1977; May et al., 1978; May & Phillips, 1979). Those results suggest that the C4-phenolate on the benzoate nucleus is more important than the C3-phenolate because inhibitors such as PHB ($K_i \approx 240$ μM) bind with higher affinity than those like MHB ($K_i \approx 4$ mM). Comparison of our structures for these two complexes indicates that the only major difference between them is that PHB^{O4} coordinates directly to the Fe^{3+} whereas the MHB^{OH3} group hydrogen bonds with Arg457 and Gln477. The ratio of K_i's suggests that PHB^{O4} coordination to the iron stabilizes the PHB complex by approximately 1.7 kcal/mol relative to the two hydrogen bonds in the MHB complex. May et al. (1978) also compared the relative inhibition of FHB and PHB and postulated that a strong hydrogen bond to the fluorine group yields an estimated $\Delta\Delta G$ of ≈3.5 kcal/mol. Accordingly, the structures for the PHB and FHB complexes suggest that the 3.0 Å $FHB^{F}\cdots Q477^{N\epsilon 2}$ hydrogen bond is primarily responsible for the increased affinity of FHB relative to PHB. Finally, the pH-dependent inhibition of MHB, PHB, FHB, and CHB (May et al., 1978; May & Phillips, 1979) indicates that their relative affinity is not related exclusively to the phenolic pK_a of each inhibitor (Table 1). Rather, the K_i value of several 3-halo-4-hydroxybenzoates correlates better with the steric bulk of the substituents at C3. Comparison of the structures for the IHB, CHB, and FHB complexes shows that the halide is hydrogen bonded in very similar positions in each complex. The steric bulk of the iodine atom in IHB clearly prevents it from penetrating further into the active site and consequently reduces the affinity of IHB for the enzyme. In contrast, the smaller halide group on CHB and FHB allows these inhibitors to occupy the active site in similar, high-affinity orientations.

The color of 3,4-PCD as isolated and in exogenous ligand complexes arises from LMCT bands originating from the tyrosinate and phenolate ligands (Table 1). Several previous resonance Raman spectroscopic studies have established that the phenolate ring vibrations of the endogenous tyrosinates or exogenous ligands are coupled to the LMCT bands exhibited by 3,4-PCD [reviewed in Que (1989)]. Resonance Raman spectra from 3,4-PCD isolated from several species, including *P. putida* and *Brevibacterium fuscum*, have been used to characterize these bands for the uncomplexed enzyme and the PHP, MHB, PHB, CHB, and FHB complexes (Table 1) (Que, 1989; Whittaker et al., 1984; Siu et al., 1992). The crystal structures provide additional insight into the origin of the differences in energies observed for these bands. In the enzyme as isolated, Tyr408 and Tyr447 have been assigned to the 1254 and 1266 cm^{-1} resonance Raman features, respectively, in part on the basis of their sensitivity to H_2O/D_2O exchange (Siu et al., 1992). The binding of MHB does not perturb these features significantly, and no additional resonance-enhanced bands appear (Que & Epstein, 1981), suggesting that MHB does not coordinate the Fe^{3+} in complete accord with our structure.

The binding of the other four inhibitors affects the tyrosinate resonance Raman bands, and new features assigned to the exogenous phenolate appear (Felton et al., 1978; Que & Epstein, 1981; Siu et al., 1992), suggesting that these inhibitors coordinate the Fe^{3+} as our results demonstrate. In

the 3,4-PCD·PHP complex, the Tyr408 and Tyr447 ring deformation modes are observed at 1256 and 1288 cm^{-1}, respectively, while the PHP ring deformation mode is also at 1288 cm^{-1} (Siu et al., 1992). The bands from both Tyr447 and PHP were observed to be insensitive to H_2O/D_2O exchange, suggesting that the lack of hydrogen bonding yields equivalent energy resonance Raman bands for each ligand. However, our crystal structure for this complex (Figure 5d) indicates that PHP^{O4} is hydrogen bonded to Wat606 while $Tyr447^{O\eta}$ does not hydrogen bond to any solvent molecules. Moreover, $Tyr408^{O\eta}$ and PHP^{O4} each coordinate to the iron in the equatorial plane, and both form hydrogen bonds to solvent molecules, suggesting that the energy of the resonance Raman bands associated with these phenolates should be similar, contrary to the spectroscopic observation. However, our structure (see Figure 5d,D) reveals another difference between these iron ligands that may account for their different resonance Raman properties. Specifically, the position of the atom *para* to the coordinated phenolate (C1 in PHP or Cγ in Tyr408 and Tyr447) relative to their respective $Fe^{3+}-phenolate^{O}$ bond and the iron coordination geometry may differentiate the phenolate ligands. Tyr408 coordinates the iron such that the $Fe^{3+}-phenolate^{O\eta}$ bond and the Cγ atom are both approximately in the iron equatorial plane. In contrast, for Tyr447 and PHP, neither the Cγ or C1 atoms nor their $Fe^{3+}-phenolate^{O}$ bond is coplanar with either the axial or equatorial iron coordination elements, respectively. This difference in coordination may consequently result in lower-energy ring deformation modes for Tyr408 relative to either Tyr447 or PHP. Moreover, the correspondingly similar coordination mode for both Tyr447 and PHP may result in their equivalent higher-energy resonance Raman features.

This type of analysis also applies to the analysis of the resonance Raman spectrum for the 3,4-PCD·PHB complex in the context of the crystal structure. Three resonance Raman bands for this complex are observed (Table 1), indicating a unique coordination mode for each phenolate ligand. Our crystal structure for the 3,4-PCD·PHB complex (Figure 5f) shows that the coordination mode of PHB is very similar to that of Tyr408. However, the $PHB^{O4}\cdots Arg457^{N\eta1}$ hydrogen bond differentiates it from both $Tyr408^{O\eta}$ and $Tyr447^{O\eta}$ as well as the fact that PHB is not a 4-alkylphenolate like Tyr and PHP. Similar analysis may also explain the observation of only two resonance Raman-enhanced bands with unequal intensity for the CHB and FHB complexes relative to the 3,4-PCD·PHB complex (Felton et al., 1978; Que & Epstein, 1981). Our structures suggest that the additional hydrogen bond between the halide of CHB or FHB and $Gln477^{N\epsilon2}$ in these complexes (Figure 5g,h) may further shift the energy of the CHB and FHB ring deformations to match that of one of the tyrosinate ligands.

Electron paramagnetic resonance spectroscopy has been used to detect direct association between the Fe^{3+} of 3,4-PCD and ^{17}O-labeled ligands through perturbations caused by superhyperfine interactions (Orville & Lipscomb, 1989). Table 1 summarizes the EPR parameters of exogenous ^{17}O-enriched ligands or solvent for the inhibitor complexes in this report. The ^{17}O-enriched inhibitor binding results correlate perfectly with the crystal structures. Like the resonance Raman results, the EPR results support our structure-based conclusion that the C3-phenol group of MHB does not coordinate the Fe^{3+} in the 3,4-PCD·MHB complex despite easy access to an open coordination site.

^{17}O-enriched solvent has also been used in EPR studies to probe iron ligation (Whittaker & Lipscomb, 1984b; Orville & Lipscomb, 1989). These results are consistent with the current structural study in most cases. One discrepancy is the observation of an Fe^{3+} solvent molecule in the 3,4-PCD·CHB crystal structure but no detectable superhyperfine broadening of the EPR spectrum from this complex. This indicates very weak coupling between the solvent molecule and the iron and further suggests that the solvent may be a neutral H_2O ligand rather than hydroxide as in the uncomplexed enzyme. Another discrepancy arises from the observation that there is no Fe^{3+} solvent molecule observed in the 3,4-PCD·MHP crystal structure but superhyperfine broadening from ^{17}O-enriched solvent is observed for this complex. The rationale for the discrepancy is not readily apparent, although it may indicate partial occupancy by the solvent in solution.

Mechanistic Implications: Structural Mimics of Early Intermediates in Substrate Binding. Several lines of evidence suggest that the binding of substrate to 3,4-PCD involves several discrete species. (i) EPR and Mössbauer spectra show that the anaerobic 3,4-PCD·PCA complex is very heterogeneous in rapidly frozen solution samples, suggesting that substrate can occupy several binding orientations (Whittaker et al., 1984). (ii) Many monohydroxy inhibitor complexes of 3,4-PCD are also composed of several spectroscopically distinct species, although they form more homogeneous complexes than substrates. (iii) Transient stopped flow kinetics show that hydroxynicotinic acid *N*-oxide inhibitor binding to wild-type 3,4-PCD (Whittaker & Lipscomb, 1984a) and PCA binding to the Tyr447 → His mutant 3,4-PCD[5] occurs in at least four discrete steps, yielding intermediates with dramatically different spectroscopic properties. Although the complexes of this study do not directly reveal a progression of binding orientations from a low-affinity to a high-affinity orientation in one complex, we propose that the range of binding orientations for the family of substrate-like inhibitor molecules are consistent with orientations that can be reasonably expected as substrate binds to the enzyme. An important finding of the current study is that the active site facilitates high-affinity complex formation in positions that alter the trigonal bipyramidal coordination geometry in favor of octahedral geometry. If PCA follows a similar progression of binding intermediates, with the resultant structural changes to the iron coordination sphere, corresponding progressive changes in the optical properties of the enzyme would be expected, as observed. Interestingly, several of the higher-affinity inhibitor complexes in this report reveal a distortion of the iron coordination geometry in the $Fe^{3+}-Tyr447^{O\eta}$ bond. Indeed, the $|F_o| - |F_c|$ electron density for our refined 3,4-PCD·FHB complex suggests that Tyr447 in a small fraction of the enzyme population is in the alternative position observed in the PCA complex in the following paper (Orville et al., 1997). Since formation of the anaerobic PCA complex displaces the axial Fe^{3+} ligand, the FHB complex may represent a binding stage just prior to the $Fe^{3+}-Tyr447^{O\eta}$ bond dissociation. The dissociation of Tyr447 does not occur to a greater extent in this report since the monohydroxy inhibitors used cannot form chelated Fe^{3+} complexes.

[5] R. W. Frazee, A. M. Orville, K. B. Dolbeare, Y. Hong, D. H. Ohlendorf, and J. D. Lipscomb, in preparation.

The present results, therefore, suggest that it is possible for the active site of 3,4-PCD to accommodate substrate-like molecules in a range of orientations. Comparison of these structures suggests that they lead logically from an iron coordination structure like that present in the resting enzyme to that of the anaerobic substrate complex in which substrate chelates the Fe^{3+} and the catecholate functional groups are both deprotonated. The latter structure would allow O_2 to attack the electronegative substrate by an electrophilic mechanism which we have proposed to be the hallmark of the intradiol dioxygenase reaction cycle (Lipscomb & Orville, 1992). These and additional insights are discussed in the following report and provide a mechanistically relevant framework for the structural variability observed here.

ACKNOWLEDGMENT

We thank the Minnesota Supercomputer Institute for providing computational resources on the Cray Y-MP and C-90 supercomputers. Numerous insightful discussions with Dr. Lawrence Que, Jr., are gratefully acknowledged. We thank M. Vetting for assistance with the electrostatic potential calculations and E. Hoeffner for maintenance of the X-ray diffraction and computational facilities within the Kahlert Structural Biology Laboratory at the University of Minnesota.

REFERENCES

Arnez, J. G. (1994) *J. Appl. Crystallogr. 27*, 649−653.
Bernstein, F. C., Koetzle, T. F., Williams, G. J. B., Meyer, E. F., Jr., Brice, M. D., Rodgers, J. R., Kennard, O., Shimanouchi, T., & Tasumi, M. (1977) *J. Mol. Biol. 112*, 535−542.
Bull, C., Ballou, D. P., & Otsuka, S. (1981) *J. Biol. Chem. 256*, 12681−12686.
Felton, R. H., Cheung, L. D., Phillips, R. S., & May, S. W. (1978) *Biochem. Biophys. Res. Commun. 85*, 844−850.
Felton, R. H., Gordon, S. L., Sowell, A. L., & May, S. W. (1984) *Biochemistry 23*, 3955−3959.
Ferrin, T. E., Huang, C. C., Jarvis, L. E., & Langridge, R. (1988) *J. Mol. Graphics 6*, 13−27.
Fisher, C. L., Cabelli, D. E., Tainer, J. A., Hallewell, R. A., & Getzoff, E. D. (1994) *Proteins 19*, 24−34.
Frazee, R. W., Livingston, D. M., LaPorte, D. C., & Lipscomb, J. D. (1993) *J. Bacteriol. 175*, 6194−6202.
Fujisawa, H., & Hayaishi, O. (1968) *J. Biol. Chem. 243*, 2673−2681.
Fujiwara, M., & Nozaki, M. (1973) *Biochim. Biophys. Acta 327*, 306−312.
Getzoff, E. D., Cabelli, D. E., Fisher, C. L., Parge, H. E., Viezzoli, M. S., Banci, L., & Hallewell, R. A. (1992) *Nature 358*, 347−351.
Gilson, M. K., Sharp, K. A., & Honig, B. H. (1988) *J. Comput. Chem. 9*, 327−335.
Glusker, J. P. (1991) *Adv. Protein Chem. 42*, 1−76.
Hendrickson, W. A. (1985) *Methods Enzymol. 115*, 252−270.
Hendrickson, W. A., & Konnert, J. H. (1980) in *Biomolecular Structure, Function, Conformation and Evolution* (Srinvasan, R., Ed.) Vol. 1, pp 43−47, Pergamon, Oxford.
Honig, B. H., & Nicholls, A. (1995) *Science 268*, 1144−1149.
Howard, A. J., Gilliland, G. L., Finzel, B. C., Poulos, T. L., Ohlendorf, D. H., & Salemme, F. (1987) *J. Appl. Crystallogr. 20*, 383−387.
Howard, J. B., & Rees, D. C. (1991) *Adv. Protein Chem. 42*, 199−280.
Jones, T. A. (1978) *J. Appl. Crystallogr. 11*, 268−272.
Kraulis, P. J. (1991) *J. Appl. Crystallogr. 24*, 946−950.
Laskowski, R. A., MacArthur, M. W., Moss, S. D., & Thornton, J. M. (1993) *J. Appl. Crystallogr. 26*, 283−291.
Lipscomb, J. D., & Orville, A. M. (1992) in *Metal Ions in Biological Systems* (Sigel, H., & Sigel, A., Eds.) Vol. 28, pp 243−298, Marcel Dekker, Inc., New York.
May, S. W., & Phillips, R. S. (1979) *Biochemistry 18*, 5933−5939.
May, S. W., Phillips, R. S., & Oldham, C. D. (1978) *Biochemistry 17*, 1853−1860.
Michaud-Soret, I., Andersson, K. K., Que, L., Jr., & Haavik, J. (1995) *Biochemistry 34*, 5504−5510.
Ohlendorf, D. H., Weber, P. C., & Lipscomb, J. D. (1987) *J. Mol. Biol. 195*, 225−227.
Ohlendorf, D. H., Lipscomb, J. D., & Weber, P. C. (1988) *Nature 336*, 403−405.
Ohlendorf, D. H., Orville, A. M., & Lipscomb, J. D. (1994) *J. Mol. Biol. 244*, 586−608.
Orville, A. M., & Lipscomb, J. D. (1989) *J. Biol. Chem. 264*, 8791−8801.
Orville, A. M., & Lipscomb, J. D. (1993) *J. Biol. Chem. 268*, 8596−8607.
Orville, A. M., Lipscomb, J. D., & Ohlendorf, D. H. (1997) *Biochemistry 36*, 10052−10066.
Que, L., Jr. (1989) in *Iron Carriers and Iron Proteins* (Loehr, T. M., Ed.) pp 467−524, VCH, New York.
Que, L., Jr. (1993) in *Bioinorganic Catalysis (*Reedijk, J., Ed.) pp 347−393, Marcel Dekker, Inc., New York.
Que, L., Jr., & Epstein, R. M. (1981) *Biochemistry 20*, 2545−2549.
Que, L., Jr., & Ho, R. Y. N. (1996) *Chem. Rev. 96*, 2607−2624.
Que, L., Jr., Lipscomb, J. D., Zimmermann, R., Münck, E., Orme-Johnson, N. R., & Orme-Johnson, W. H. (1976) *Biochim. Biophys. Acta 452*, 320−334.
Siu, D. C.-T., Orville, A. M., Lipscomb, J. D., Ohlendorf, D. H., & Que, L., Jr. (1992) *Biochemistry 31*, 10443−10448.
Smith, R. H., & Martell, A. E. (1989) in *Critical Stability Constants*, Vol. 6, Plenum Press, New York (supplemental no. 2 and earlier volumes).
True, A. E., Orville, A. M., Pearce, L. L., Lipscomb, J. D., & Que, L., Jr. (1990) *Biochemistry 29*, 10847−10854.
Whittaker, J. W., & Lipscomb, J. D. (1984a) *J. Biol. Chem. 259*, 4476−4486.
Whittaker, J. W., & Lipscomb, J. D. (1984b) *J. Biol. Chem. 259*, 4487−4495.
Whittaker, J. W., Lipscomb, J. D., Kent, T. A., & Münck, E. (1984) *J. Biol. Chem. 259*, 4466−4475.
Whittaker, J. W., Orville, A. M., & Lipscomb, J. D. (1990) *Methods Enzymol. 188*, 82−88.

BI970468N